Modelling of a solenoid injector for internal combustion engines and simulation using the bond graph methodology

Jessica Gaucherand[a], Eilif Pedersen[b], Corinna Netzer[a], Terese Løvås[a]

[a]Department of Energy and Process Engineering, Norwegian University of Science and Technology, Kolbjørn Hejes vei 1a, Trondheim, 7491, Trøndelag, Norway. [b]Department of Marine Technology, Norwegian University of Science and Technology, Marinteknisk senter, Otto Nielsens veg 10 Trondheim, 7052, Trøndelag, Norway.

Author Accepted Manuscript version of the paper by Jessica Gaucherand in SAE Technical Paper 2023-01-0195, 2023, DOI https://doi.org/10.4271/2023-01-0195.

Abstract

In internal combustion engines, fuel injection timing, injection rate and pressure is optimized to ensure suitable combustion and reduce emissions. Injectors are complex systems where mechanical, electromagnetic, and fluid dynamics interact together. Numerical model development of injectors allows for investigating different conditions, as well as optimization of the system in a safe manner. In this study, a 1-dimensional (1D) mathematical model of a direct gasoline injector (GDI) is presented, supported by computational fluid dynamics (CFD) in-nozzle flow simulations. The described system is a commercially available injector where the internal geometry was captured using silicone molds of the nozzle. The model includes the representation and interaction of the different components across several domains using the bond graph methodology. In the injector, the needle is magnetic and is lifted when an electromagnetic field is activated. When the magnetic force becomes stronger than the spring force and the fuel's pressure pushing the needle downward, the needle lifts and fuel flows through the nozzle and out of the injector. These motions are described by the mathematical model, for which the magnetic signal serves as input. The model output provides the needle lift and information on the fluid flow, including the pressure, temperature, and mass flow rate. Gaseous methane and liquid ammonia injection are investigated in separate models where the thermofluid part of the model is changed to account for a compressible gas, which in turn follows the perfect gas law in one case, and an incompressible liquid in the other case. Comparison with literature shows that the model captures the dynamics of the needle lift well, and the mass flow is accurately predicted.

Introduction

Gasoline direct injectors (GDI) are used to directly inject fuel into the combustion chamber of internal combustion engines. The use of GDIs increases engine efficiency, allowing fuel savings and the reduction of emissions, especially unburned hydrocarbons [1] [2]. The understanding of the dynamic of fuel injectors is important for optimizing their use in engines and achieving the best operating conditions. However, prototyping and testing in the laboratory is an expensive process. Therefore, using computational resources and models is interesting to develop injectors and simulate their behavior and performances. The injection pressure and temperature of the fuel at the injector's exit are valuable information for further evaluating the combustion process using computational fluid dynamics (CFD). These features, coupled with injector position, angle, and geometry, will impact the nature of the spray inside the engine. Although the pressure and temperature of the fuel can be known in the reservoir, their evolution in the supply tube and the injector is not straightforward to measure experimentally. The added value of numerical simulations is to predict these fluid properties at the injector's exit with better accuracy, especially the pressure and temperature. 3D CFD modeling of complex geometries such as the one of an injector is, however, computationally expensive to perform and only focuses on the injector part and not on the supply lines and reservoir conditions. On the other hand, 1D models are computationally inexpensive and can be used to model the injectors dynamics. This way, parametric studies can be efficiently performed for optimization purposes and rapid testing under various conditions. Mathematical models of injectors have been developed in the past. Reverse engineering of an injector was performed by Krivopolianskii et al. [3] to avoid destroying the injector to evaluate its geometry by developing a model and comparing the injection rate with experimental data. For example, Æsøy and Pedersen [4] use the bond graph methodology for a servo-valve activated injector. A solenoid injector model with the bond graph methodology has also been developed by Bai et al. [5] but does not account for the pressure and temperature of the fuel at the injector exit. Mathematical models of GDIs using dynamic response analysis have been developed to optimize injector drive circuits such as Tsai and Zhan [6] or to optimize the needle oscillations such as Yao et al. [7]. A mathematical model coupled with CFD was developed by Zhang et al. [8] but did not account for the fuel temperature evolution. Payri et al. [9] used the same technique that we will present in Section 3 to characterize the internal geometry of a diesel injector, then developed an AMESim mathematical model of the injector and compared results with experimental data, finding good agreement of the injection rate between the two. The work presented here is a step towards filling the gap by accounting for the fuel's velocity, temperature and pressure at the nozzle exit in a 1D model of an injector. This work aims to contribute to decarbonizing internal combustion engines and gain further insights into a carbon-free fuel. Indeed, recent work on ammonia (NH_3) has shown its potential as a fuel in internal combustion engines [10, 11, 12]. The paper starts by detailing the internal geometry and the operation of the GDI. The model components are introduced separately, and the model assembly is presented. The first step is modelling the injector's electromagnetic and mechanical parts using the bond graph methodology. In this study, the injection is first assumed to be gaseous employing the perfect gas law. Next, a hydraulic model replaces the gas flow model to study the injection of liquid fuels such as ammonia. Three-dimensions CFD simulations are performed using Reynolds-averaged Navier–Stokes simulation in order to evaluate a realistic value of the discharge coefficient for the one-dimension (1-D) model. In the last part of the paper, simulations of the model dynamics are performed.

GDI description

A 6-hole high-pressure solenoid injector, the HDEV5, is considered in this study. The injector is available in two versions with varying lengths, however in this work only the long injector is considered. In order to develop a representative model, the determination of the internal geometry of the injector is done in two parts: internal geometry of the injector body and characterization of the nozzle holes. The procedure developed by Macian et al. [13] is used to characterize the nozzle with a slight variation of the technique. Indeed, a mold needs to be taken from the outside to provide the counterbore's measurements. Several silicone molds were created for repeatability and error measurements. These were coated in gold in order to be put through a scanning electron microscope (SEM). Pictures were taken to determine the internal geometry, and the nozzle head's computer-aided design (CAD) model was developed as shown in Fig.1.

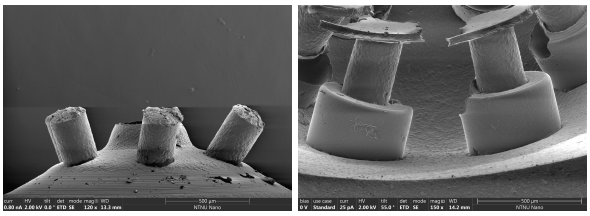

(a) Internal mold of GDI nozzle head viewed with electron microscope.

(b) External mold of GDI nozzle head viewed with electron microscope.

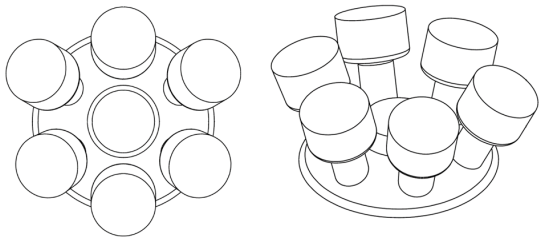

(c) CAD model of nozzle head reproduced from electron miscroscope pictures and measurements.

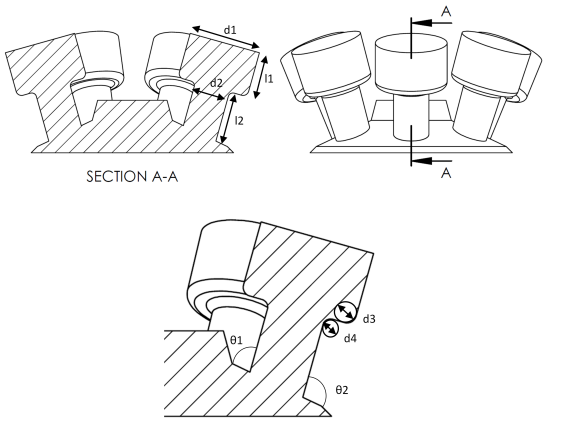

(d) CAD model of nozzle head reproduced from electron miscroscope pictures and measurements, sectioned view.

Figure 1: Silicone molds with electron microscope and CAD model of GDI nozzle head.

The GDI is made of a series of chambers of various diameters, as illustrated in Fig. 2. The needle, depicted with 3, 4, and 5 in Fig. 2 is magnetic and is lifted when an electromagnetic field is activated. The magnetic force becomes more substantial than the spring (2) and the fuel's pressure force pushing the needle downward. The coil inducing the electromagnetic field is inside the armature (1). The needle lifts, and the fuel flows around the needle into the sac and out the holes (6). The arrows in Fig. 2a show the flow path inside the injector. The top of the injector is linked to the supply line that draws the fuel from the pressurized tank (the supply line and tank are not pictured here).

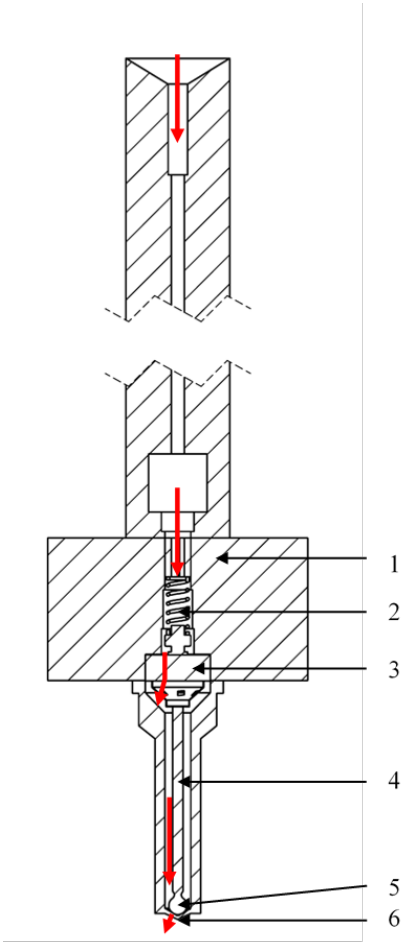

(a) CAD model of full injector body with fluid path. The arrows point to the following elements: 1- Armature, 2- Spring, 3 to 5- Needle, 6- Injector's holes

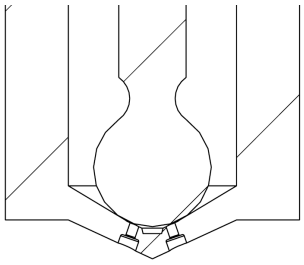

(b) CAD model of a zoom of the nozzle head and needle end.

Figure 2: CAD model of the GDI internal geometry.

Injector model

The bond graph methodology is an energy based mathematical modelling approach for multi-physics systems [14]. The key concept of bond graphs is the use of power bonds representing the energy flow, i.e. the power between the components or physical phenomena. A power bond connects the components and has two variables: effort

and flow. A total of nine elements are needed to model the energy flow in physical systems:

- Sources of effort (Se) and flow (Sf),
- Storage elements: the capacitor (C) and the inertia (I),
- Dissipative element: the resistance (R),
- Energy converters elements: the gyrator (GY) and the transformer (TF),
- Junctions: conserves flow (1-junction) or energy (0-junction).

The simulation software 20-sim [15] is used to model and simulate the dynamics of the injector. The model is divided into three parts:

- The electromagnetic subsystem for the solenoid,
- The mechanical subsystem for the needle's dynamic,
- The thermo-fluid system for the fuel path.

The fuel injection system requires the assembly of the three submodels to form a complete model. The flowchart Fig. 3 illustrates the interaction between the different parts of the system. The fuel flow in the injector is a complex assembly of chambers and sections with diameter changes, as shown in Fig. 2a. The electromagnetic subsystem acts on the needle dynamic over which other forces apply, including the pressure from the fuel. As the needle lifts, a signal changes the area of passage of the valve. The fuel, therefore, flows around the needle into the holes. A large number of chambers in the GDI can be simplified to limit the number of C- and R-elements in the system in order to describe the flow model without impacting the flow's properties. We will first present an overview of the model fully assembled then detail the different parts of each submodels.

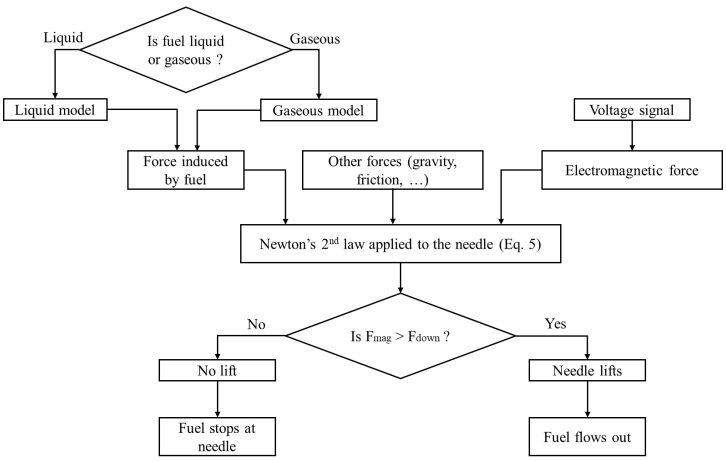

Figure 3: Flowchart of the model of the injector operation.

Model assembly

Figure 4 presents the complete model for the gaseous case with the assembly of the three submodels (electromagnetic, mechanical and thermo-fluid) and their links.The discharge coefficient for the junction inside the injector is 0.8 to account for the junction's geometry and the pressure losses. Pipe models are needed where the geometry of the injector is long enough for a pressure wave to travel compared to the time necessary for the fuel to be injected. The pipes allow for inspecting the pressure wave's effect on the injected fuel. 20-sim derives the state equations from the bond graph, and the simulation can be performed. At the nozzle head, the geometry of the holes requires a different discharge coefficient. Three dimensional (3D) computational fluid dynamics (CFD) analysis can give a more precise description of the flow behavior at the end of the nozzle, and identify the effect of the geometry on possible cavitation events happening in the nozzle head. The methodology to obtain the coefficient at the nozzle is described in the last part of this Section.

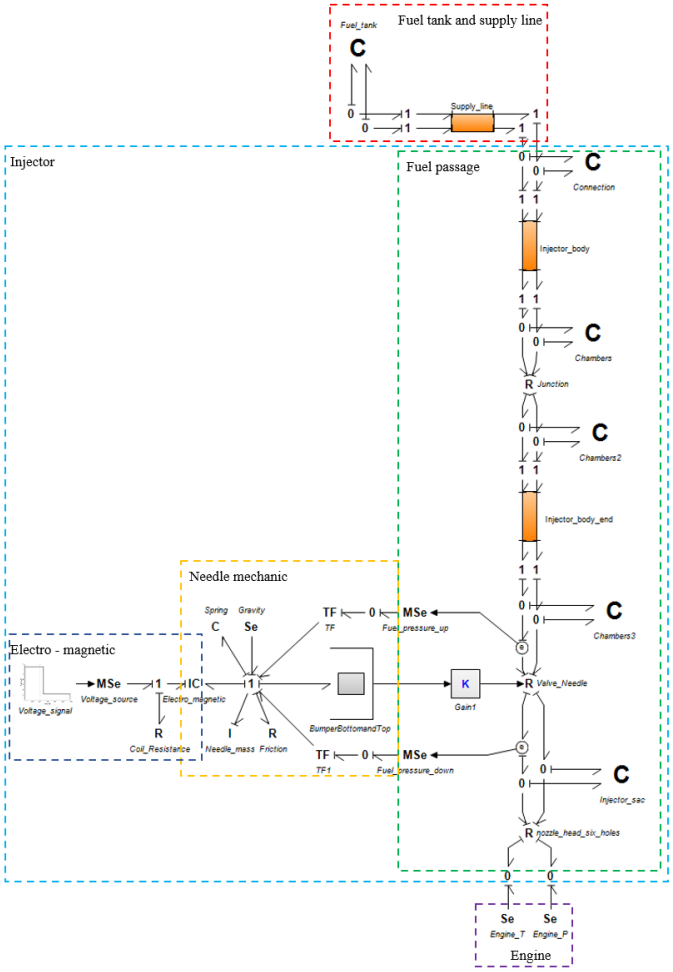

Figure 4: Bond graph representation of the full system. The red box represents the tank and the supply line, the light blue box represents the injector with the three submodels (dark blue for electro-magnetic, yellow for mechanical, and green for thermo-fluid submodel), and the purple box represents the combustion chamber.

Electromagnetic subsystem

The electromagnetic subsystem controls the needle lift. When the current flows through the coil inside the armature, it is energized, and a closed magnetic path is formed, lifting the movable magnetic needle. The input to this subsystem is the manufacturer-provided voltage for the pulse. In this study, a single pulse is considered. A peak voltage source of 65 V is provided with duration of 480 µs, followed by a holding voltage of 12 V with a duration of 704 µs. The injector coil has a resistance of 1.5 Ω. In bond graph modeling, the electromagnetic solenoid behaves like an inductor on the electrical side. On the mechanical side, the device acts like a spring [16]. A multiport-IC element is therefore needed to complete the model of the subsystem, see Fig. 5. On the electric side, the effort variable is the electric potential. The flow variable is the current. On the mechanical side, the effort variable is the force, and the flow variable is the velocity. λ is the flux linkage and x the displacement. Two constitutive laws are needed to build the multiport; one for the current (i), Eq. 1, and one for the force (F_{mag}), Eq. 2, both as functions of

the flux linkage and of the displacement:

$$i = \frac{\lambda}{L(x)}, \tag{1}$$

$$F_{mag} = -\frac{\lambda^2}{2}\frac{\partial L(x)/\partial x}{L(x)^2} = \frac{i^2}{2}\frac{\partial L(x)}{\partial x}, \tag{2}$$

where $L(x)$ is the position-dependent inductance of the coil. $L(x)$ is obtained as in [8]:

$$L = \frac{N^2 \cdot \mu_1 \cdot \frac{\pi}{4} \cdot d^2 \cdot h}{\frac{d \cdot w}{2} + \Delta x \cdot h} \tag{3}$$

with N being the number of coil turns, μ_1 the permeability in the air in [H/m], d the diameter of the metallic needle attachment, w the non-magnetic strip between the coil and the attachment, h the height of the attachment, and Δx the variable air gap. The evolution of the magnetic force and the supply voltage are shown in Fig. 6. The electromagnetic force first increases when the 65 V pulse is applied. Then the force decreases, and we see two elbows; the first is caused by the interruption of the voltage supplied, and the second is due to the needle closing since the inductance is position-dependent.

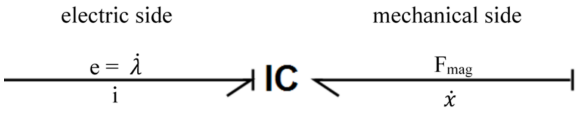

Figure 5: Bond graph representation of the multiport-IC to model the electromagnetic solenoid, to link the electrical current and the magnetic force acting on the needle.

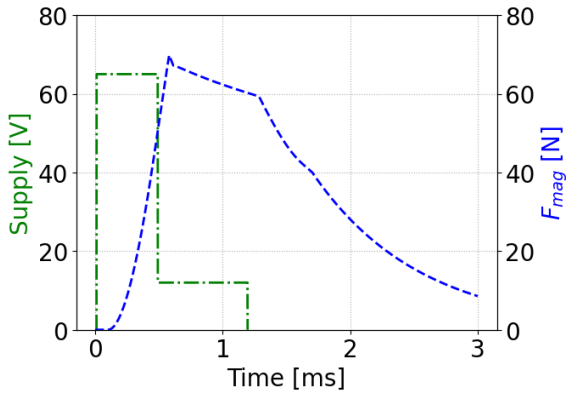

Figure 6: Supply electric potential signal (green dashed-dotted line) and resulting electromagnetic force (blue dashed line) for the electromagnetic subsystem.

The complete electromagnetic submodel flow chart is pictured in Fig. 7.

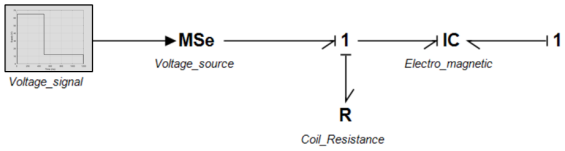

Figure 7: Bond graph representation of the complete electromagnetic submodel, including the input voltage, the coil resistance and the multiport-IC element.

Mechanical system

The mechanical system dictates the needle's dynamics. Forces acting on the needle are the following: force from the spring (see (2) Fig. 2), friction, gravity, magnetic force, and pressure from the fuel, as pictured in Fig. 8. The force acting on the needle from the fuel pressure (F_{fuel}) is calculated with a transformer element, with the equation:

$$F_{fuel} = P_{fuel} \cdot A \tag{4}$$

The area A accounting for the needle surface affected by the fuel pressure P_{fuel} is calculated using the developed CAD model. Bumpers at the top and bottom of the needle trajectory block the needle movement when it is at the position $x > x_{max}$ or $x < 0$. The 1-junction describes the needle's velocity, and is a form of Newton's second law since it is linked to an I-element for the mass, as pictured in the graphical model Fig. 9. From the graphical model, the equation for the needle dynamic can be extracted:

$$I\ddot{x} - R\dot{x} + \frac{1}{C}x = F_{\text{mag}}(t) + P_{\text{fuel up}}\,A_{\text{fuel up}}\,(x) + P_{\text{fuel down}}A_{\text{fuel down}}\,(x) + F_{\text{bumper}}(x) \tag{5}$$

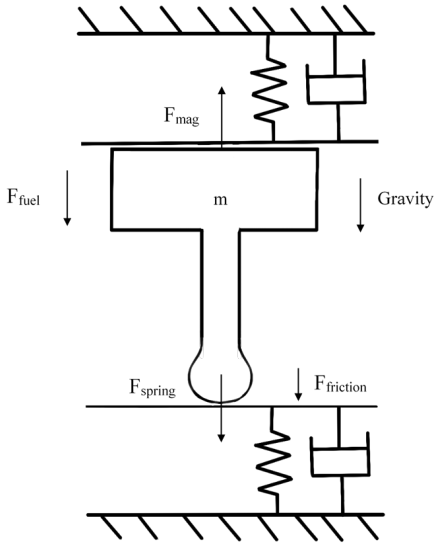

Figure 8: Illustration of mechanical system with acting forces on the needle: magnetic force, gravity, fuel pressure, friction, spring force. Bumpers at each end of the trajectory are also included in the illustration.

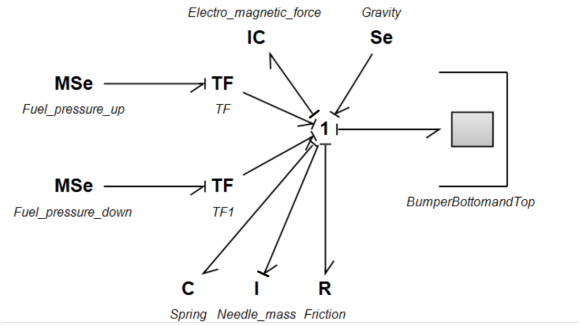

Figure 9: Bond graph representation of the complete mechanical submodel.

The needle is lifted when the electromagnetic force becomes stronger than the downward force. The needle can only lift 0.07 mm due to the

injector's geometry. As it lifts, the fuel flows around the needle head and through the nozzle holes into the combustion chamber in the engine. The needle acts as a variable area valve for the flow.

Thermo-fluid system

Using the bond graph method, developing the fuel flow model requires a different approach than the standard methodology. Karnopp et al. [17] introduced pseudo-bond graphs to model thermodynamic systems. A double bond is used, where the effort pressure P is paired with the mass flow rate $\dot{m}$ and the effort temperature T is paired with the energy flow rate $\dot{E}$ to link two bond-graphs elements as seen in Fig. 10. The state variables become the total mass m and the total energy E.

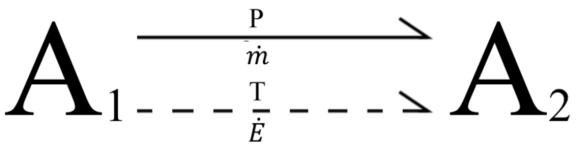

Figure 10: Bond graph representation of thermo-fluid pseudo bonds between two bond graph elements. A double bond is used, the top bond represents the pressure and mass flow rate effort/flow pair and the bottom bond represents the temperature and energy flow pair.

Building blocks are needed to represent the thermo-fluid components: accumulators, restrictions, and pipes. The structure of these blocks will be described hereafter. Two models are developed, one for gaseous fuel injection and the other for liquid fuel injection.

Gaseous fuel

In this paragraph, we consider a fuel in the incompressible gas phase.

Accumulators (C-element) Control volumes with input (subscript in) and output (subscript out) flows are represented in bond graph models with a C-element that is called an accumulator. An accumulator for the gas phase follows mass and energy conservation laws, and these are its state equations :

$$\frac{d}{dt}m = \dot{m}_{in} - \dot{m}_{out}, \tag{6}$$

$$\frac{d}{dt}E = h_{in}\dot{m}_{in} - h_{out}\dot{m}_{out} - P\frac{dV}{dt}, \tag{7}$$

with h the enthalpy and V the accumulator's volume. We consider constant volume in the accumulators, so $\frac{dV}{dt} = 0$. Relations are needed to link the state variables and the effort. Here we follow the perfect gas law :

$$P = \frac{mRT}{V}, \tag{8}$$

with R the gas constant defined Eq. 10,

$$T = \frac{E}{mC_v}. \tag{9}$$

The heat capacities at constant pressure and constant volume, C_p and C_v are properties of the gas. We assume, in this model, that they are constants in the ranges of pressure and temperature investigated and are computed using the NIST thermodynamic database [18].

$$R = C_p - C_v, \tag{10}$$

$$\gamma = \frac{C_p}{C_v}. \tag{11}$$

An accumulator model can be developed using pseudo-bond graphs and a 0-junction to translate the effort conservation at the interface, as pictured Fig. 11.

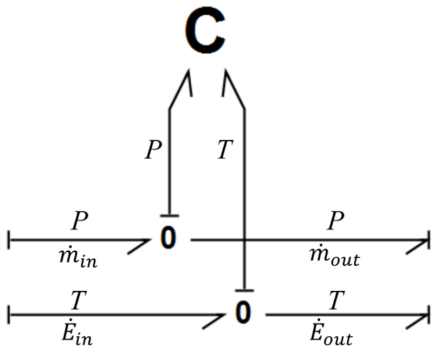

Figure 11: Bond graph representation of the accumulator (C-element) model. Effort variables of the power bonds pressure and temperature are conserved.

Heat transfer to account for conduction can be added, as introduced by Karnopp et al.[17]. Variable volumes can also be modeled, or one can use multi-component accumulators with multiphase [19]. The simplest model for an incompressible gas is however sufficient for this study's purpose.

Restrictions (R-element) Flow restrictions are helpful building blocks for thermodynamic systems. These represent nozzles or valves where there is no storage of fluid but which impact the effort variable due to the geometry of the passage. An R-element can model the restrictions, such as an isentropic nozzle. We first need to derive the mass flow and energy flow. The mass flow for an isentropic flow depends on the ratio of the upstream (subscript u) and the downstream (subscript d) pressure in the nozzle:

$$P_r = \frac{P_d}{P_u}. \tag{12}$$

When $P_r > P_c$, where P_c is a critical pressure defined Eq. 15, then:

$$\dot{m} = A\frac{P_u}{\sqrt{T_u}}\sqrt{\frac{2\gamma}{R(\gamma-1)}}\sqrt{P_r^{2/\gamma} - P_r^{(\gamma+1)/\gamma}}. \tag{13}$$

Otherwise, when $P_r < P_c$, then

$$\dot{m} = A\frac{P_u}{\sqrt{T_u}}\gamma\left(\frac{2}{\gamma+1}\right)^{\frac{\gamma+1}{2(\gamma-1)}} \tag{14}$$

with :

$$P_c = \left(\frac{2}{\gamma+1}\right)^{\gamma/(\gamma-1)}. \tag{15}$$

The energy flow $\dot{E}$ is determined by

$$\dot{E} = C_p T_u \dot{m}. \tag{16}$$

The sign of $\dot{m}$ and the upstream and downstream sides of the nozzle are dictated by the pressure drop ΔP across the nozzle.

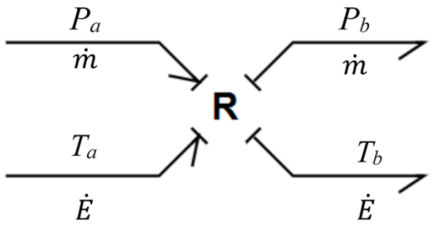

Figure 12: Bond graph representation of the restriction (R-element) model. Flow variables of the power bonds mass flow rate and energy flow are conserved.

Figure 12 shows the R-element component. Inputs for the component are P_a, P_b, T_a, and T_b, and outputs are $\dot{m}$ and $\dot{E}$. The procedure is as follow :

$$\begin{aligned} &\text{if } P_a > P_b, \text{ then } P_u = P_a, \quad T_u = T_a, \quad P_d = P_b, \\ &\text{if } P_a < P_b, \text{ then } P_u = P_b, \quad T_u = T_b, \quad P_d = P_a. \end{aligned} \tag{17}$$

P_u and P_d are assigned using Eq. 17, then P_r is computed using Eq. 12. Then the mass flow is computed using Eq. 13 or Eq. 14 depending on the value of P_r. If $P_a > P_b$ then the mass flow is as computed, otherwise, the mass flow becomes $-\dot{m}$. Finally, Eq. 16 is used to compute the energy flow $\dot{E}$. A variation on the model exists with a variable area to account for a valve position or multi-component fluid as in [19]. The valve position variation requires a signal to modify $\dot{m}$. This model uses a variable area valve where the needle head is. When the needle lifts, the area where the fuel will flow increases. When the needle is resting to close the injector, the signal is zero to indicate that no flow is going to the combustion chamber.

Pipes Lastly, a pipe model accounts for unsteady flows and for the pressure waves across long pipe sections. Navier Stokes equations for a one-dimensional flow are used in this building block for the mass, energy, and momentum conservation equations. The pipe model is described by Strand et al. in [20]. To obtain the state equation, we divide the pipe into N control volumes (Fig. 13). We assume constant density, temperature, and velocity within each control volume i.

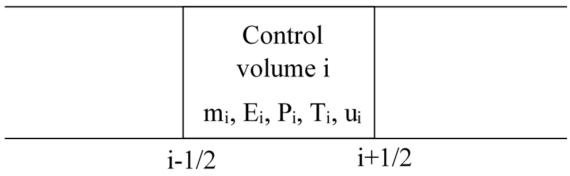

Figure 13: Illustration of control volume i.

We integrate the Navier-Stokes equations over one control volume and find the equations for the mass, momentum and total energy conservation:

$$\frac{dm_i}{dt} = \dot{m}_{i-1/2} - \dot{m}_{i+1/2}. \tag{18}$$

$$\begin{aligned} \frac{d(mu)_i}{dt} =& \dot{m}_{i-1/2} u_{i-1/2} + P_{i-1/2} A - \dot{m}_{i+1/2} u_{i+1/2} \\ &- P_{i+1/2} A - \frac{\lambda}{2D} m_i \left| u_i \right| u_i. \end{aligned} \tag{19}$$

$$\begin{aligned} \frac{dE_i}{dt} =& \dot{m}_{i-1/2} \left(h_{i-1/2} + \frac{1}{2} u_{i-1/2}^2 \right) \\ &- \dot{m}_{i+1/2} \left(h_{i+1/2} + \frac{1}{2} u_{i+1/2}^2 \right) + \dot{Q}_i. \end{aligned} \tag{20}$$

Here, u is the velocity, A is the cross-section area of the pipe, λ is a friction coefficient, D is the pipe's diameter, and $\dot{Q}$ is a heat source. The effort variables, pressure, temperature and velocity over the control volume i can then be computed:

$$\begin{aligned} P_i &= \frac{(\gamma - 1)}{\Delta x_i A} \left(E_i - \frac{1}{2} \frac{(mu)_i^2}{m_i} \right). \\ T_i &= \frac{1}{c_v} \left(\frac{E_i}{m_i} - \frac{1}{2} \frac{(mu)_i^2}{m_i^2} \right). \\ u_i &= \frac{(mu)_i}{m}. \end{aligned} \tag{21}$$

The flow at the boundary and at the adjacent control volumes still needs to be computed. This is done by accounting for the fluid's flow stronger dependency on the upstream condition by using a Mach-modulated approach:

$$g_{i+1/2} = \frac{1}{2} \left(g_i + g_{i+1} \right) + \frac{1}{2} f\left(M_u \right) \text{sign}\left(u_u \right) \left(g_i - g_{i+1} \right). \tag{22}$$

where u_u and M_u are the velocity and Mach number in the control volume upstream of the boundary.

$$f\left(M_u \right) = M_u^r \in [0, 1]. \tag{23}$$

r is a real positive constant that has been tuned for a wide range of application based on robustness, accuracy and computational speed optimization. Values for r are [2, 2, 0.01, 0.0001] for the velocity, pressure, density and temperature [20]. In terms of bond graph interpretation, three bonds are needed: pressure with mass flow, temperature with energy flow, and force due to pressure and convected momentum with the average fluid velocity as illustrated in Fig. 14.

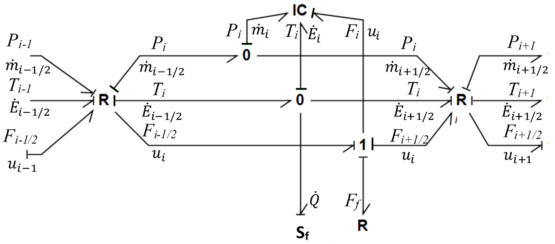

Figure 14: Bond graph representation of pipe control volume i.

A three port IC-field is needed as the conservation of mass and total energy act as a C-element, but the momentum is related to the inertia of the fluids and is related to an I-element. The equations for the IC-field are:

$$\begin{aligned} P_i &= \Phi_{IC_P}\left(m_i, (mu)_i, E_i \right), \\ T_i &= \Phi_{IC_T}\left(m_i, (mu)_i, E_i \right), \\ u_i &= (mu)_i / m_i. \end{aligned} \tag{24}$$

The constitutive equations for the R-element between the control volumes i and $i+1$ are:

$$\begin{aligned} \dot{m}_i &= \rho_i u_i A, \\ \dot{E}_i &= \dot{m}_i \left(h_i + \frac{1}{2} u_i^2 \right), \\ F_i &= P_i A + \dot{m}_i u_i. \end{aligned} \tag{25}$$

Density ρ_i, and velocity u_i are computed with Eq. 22

The R-element in Fig. 14 corresponds to the frictional force, and the Sf-element corresponds to the heat flow added to the control volume. This source is not present in an adiabatic case, which is what we will consider in our model. The pipe needs to be connected to other submodels to account for pressure and temperature at the boundaries. The last bond for velocity ends at the R-element located at the pipe model's extremity, as illustrated in Fig. 15.

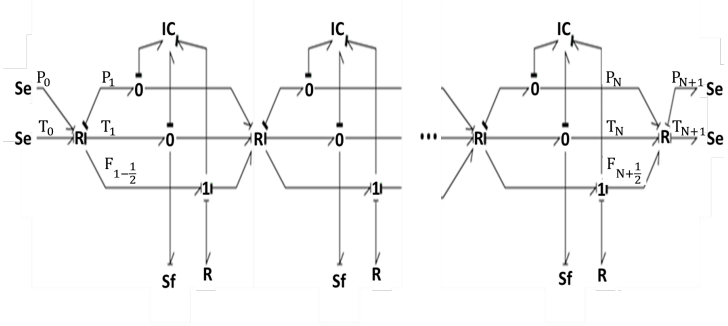

Figure 15: Bond graph representation of complete pipe model with boundary conditions.

Liquid fuel

In this paragraph we consider a liquid fuel. Equations of state are needed to obtain properties such as ρ, enthalpy, etc. One approach is to use equations of state for fluids such as Peng-Robinson or to use thermodynamic tables where the properties have been calculated using these equations of state. We use REFPROP [21], the NIST reference database for thermodynamics and transport properties of fluids.

Accumulators (C-element) We consider a constant volume in the accumulators, so $\frac{dV}{dt} = 0$. Constitutive equations are needed to link the state variables and the effort:

$$P = \phi_P(\rho, e), \tag{26}$$

$$T = \phi_T(\rho, e). \tag{27}$$

The functions ϕ_P and ϕ_T are used when the model refers to a thermodynamic table and the values of pressure and temperature are obtained based on the values of density ρ and the specific internal energy e. The values of ρ and e are obtained in the following way: first, the initial values of ρ and e (respectively, ρ_0 and e_0) are determined using the initial conditions of temperature and pressure in the accumulator :

$$\rho_0 = \phi_\rho(P_0, T_0), \tag{28}$$

$$e_0 = \phi_e(P_0, T_0), \tag{29}$$

$$m_0 = \rho_0 V, \tag{30}$$

with V the volume of the accumulator. The initial energy E_0 is given by

$$E_0 = u_0 m_0, \tag{31}$$

It follows then that

$$m = \int \dot{m} + m_0, \tag{32}$$

$$E = \int \dot{E} + E_0, \tag{33}$$

and it holds that

$$\rho = \frac{m}{V}, \tag{34}$$

$$e = \frac{E}{m}. \tag{35}$$

A model of the accumulator can be built using pseudo bond graphs and a 0-junction to translate the effort conservation at the interface as shown in Fig. 11.

Restrictions (R-element) An R-element can, as described above, model flow restrictions. As for gas phase we first need to derive the mass flow and energy flow. The mass flow for a nozzle depends on the pressure difference upstream (P_u) and downstream (P_d) the nozzle [22] :

$$P_r = P_u - P_d. \tag{36}$$

When $P_r > 0$, then :

$$\dot{m} = AC_d \sqrt{\frac{2}{\rho}(P_u - P_d)} \tag{37}$$

and the total energy flow is :

$$\dot{E} = \dot{m} h \tag{38}$$

with h being the specific enthalpy. h and ρ are obtained using the thermodynamic tables

$$h = \phi_h(T_u, x), \tag{39}$$

$$\rho = \phi_\rho(T_u, x) \tag{40}$$

where x is the fraction of vapour. In our study, it will be zero as we consider only liquid state. Figure 12 shows the R-element component.

Pipes Finally, a pipe model helps model unsteady flows along long pipes. A distributed parameter element approach is used, similar to the method described by Æsøy and Pedersen [4] and Lebrun[23] for the hydraulic flow model. The pipe does not account for the temperature, only pressure is accounted for to represent the pressure wave propagation. The method followed here is the modal approach, consisting of solving partial differential equations. Thoma et al. [24] showed that only three modes were needed in the modal approach to obtain accurate results. The partial differential equations to solve are the following:

$$\begin{aligned} \frac{1}{\rho}\frac{\partial P}{\partial x} + \frac{1}{A}\frac{\partial Q}{\partial t} + \frac{FQ}{A} &= 0. \\ \frac{c^2}{A}\frac{\partial Q}{\partial x} + \frac{1}{\rho}\frac{\partial P}{\partial t} &= 0. \end{aligned} \tag{41}$$

with A being the cross sectional area of the pipe, Q the flow rate, c the wave speed, and F the loss coefficient found using the Hagen-Poiseuille flow theory. Second derivation is applied for t and x to eliminate pressure or flow:

$$\begin{aligned} \frac{\partial^2 Q}{\partial t^2} + F\frac{\partial Q}{\partial t} - c^2\frac{\partial^2 Q}{\partial x^2} &= 0, \\ \frac{\partial^2 P}{\partial t^2} - F\frac{\partial P}{\partial t} - c^2\frac{\partial^2 P}{\partial x^2} &= 0. \end{aligned} \tag{42}$$

The orthogonality of the modal functions allows getting a set of decoupled ordinary differential equations for each normal mode. We thus obtain the following:

$$\begin{aligned} \frac{\rho}{A}\frac{\partial^2 Q}{\partial t^2} + \frac{\rho F}{A}\frac{\partial Q}{\partial t} - \frac{\rho}{A}c^2\frac{\partial^2 Q}{\partial x^2} &= \dot{P}_0\delta(0) + \dot{P}_L\delta(L) \\ \frac{A}{\rho c^2}\frac{\partial^2 P}{\partial t^2} + \frac{AF}{\rho c^2}\frac{\partial P}{\partial t} - \frac{A}{\rho}\frac{\partial^2 P}{\partial x^2} &= \dot{Q}_0\delta(0) + \dot{Q}_L\delta(L) \end{aligned} \tag{43}$$

with P_0, P_L, Q_0 and Q_L, being the pressure and mass flow at each end of the pipe, and δ the Dirac function. For the i_{th} normal mode, the first equation of Eq. 43 is solved. The inertia, capacitance and resistance for the i_{th} mode are in Table 1. The bond graph representation of the modal pipe model is shown in Fig. 16.

Table 1: Capacitance, resistance and inertia for the normal mode i.

	C	R	I
i = 0	$C_0 = \infty$	$I_0 = \frac{\rho L}{A}$	$R_0 = \frac{8\nu\rho L}{A^2}$
i = 1,2,..., N	$C_0 = \frac{2AL}{\beta_{eq}(\pi i)^2}$	$I_i = \frac{I_0}{2}$	$R_i = \frac{R_0}{2}$

With L the pipe's length and ν the fluid's kinetic viscosity. The fluid bulk modulus β is given by $\beta_{eq} = \left(\frac{1}{\beta} + \frac{1}{t_w E_v}\right)^{-1}$ where t_w is the pipe wall thickness and E_v is Young's modulus of elasticity of the wall material.

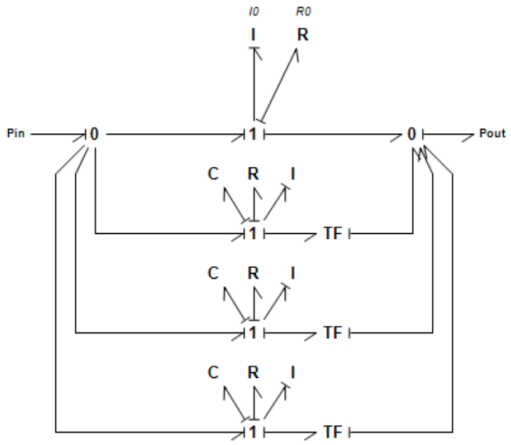

Figure 16: Bond graph representation of the modal pipe model.

Since the pipe model only accounts for pressure evolution, it is linked to the accumulator models as illustrated in Fig. 17, with a bond only on the pressures.

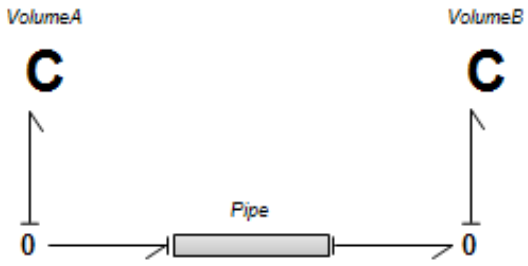

Figure 17: Bond graph representation of the pipe model linked to the accumulator model by the pressures.

Discharge coefficient using 3-D CFD

The objective of the paper is to use a one dimensional model to do rapid testing of an injector. However, for more precise information, three dimensional fluid dynamics simulation can support the model development. A discharge coefficient can be determined from CFD of the in-nozzle flow [25]. In this study, CONVERGE 3.0 [26] is used to simulate the flow in the HDEV5 injector, using the same CAD model as described Fig. 1 and Fig. 2. The Eulerian framework is used for solving the momentum, mass, energy and species conservation equations. A Reynolds averaged Navier Stokes formulation is used for closure for the turbulence model: the standard k-ϵ model. A volume of fluid (VOF) method is used to simulate multiphase flow and also a cavitation model is employed [27], [28]. The model captures the phase change from liquid to vapor inside the injector. A Cartesian mesh is automatically generated during the simulation process, with refined mesh near the nozzle. This 3D transient simulation provides information about the amount of vapor forming in the injector when in this case liquid ammonia is injected. This is especially useful in the liquid fuel one dimensional model.

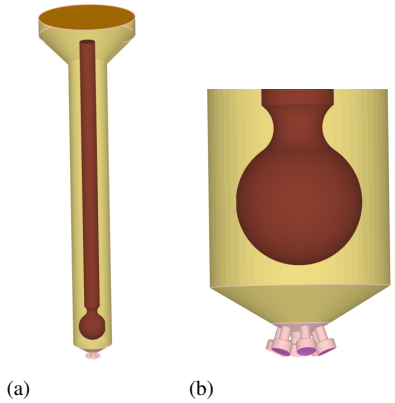

Figure 18: Geometry of the simulated injector: full injector and zoom on the nozzle head.

At the inlet, liquid ammonia at a temperature of 300 K and a pressure of 200 bar enters the domain. At the outlet, varying pressures at a temperature of 300 K are imposed. The rest of the domain is composed of walls following the law-of-the-wall boundary condition for velocity, and the heat transfer model is set to O'Rourke and Amsden [29]. The needle inside the injector is a moving wall with a translating motion up and down. The needle movement mimics open and closed conditions during which the fuel is either injected or not injected into the combustion chamber. Longer injection timings were chosen (0.3 ms) to ensure that steady state was reached during the injection. The discharge coefficient C_d is defined as the ratio between the theoretical ideal liquid mass flow rate through the outlet and the actual liquid mass flow rate. The theoretical liquid mass flow rate is determined using the following formula based on Bernoulli's equation:

$$\dot{m}_{ideal} = A\sqrt{2\rho\Delta P} \tag{44}$$

with A being the nozzle outlet area, ρ the inlet density, and ΔP the difference between the upstream and downstream pressure. The discharge coefficient is defined as:

$$C_d = \frac{\dot{m}_{real}}{\dot{m}_{ideal}} \tag{45}$$

with $\dot{m}_{real}$ as the computed mass flow rate of liquid ammonia through the outlet. To obtain the liquid mass flow rate, the fraction of liquid at the outlet can be computed using the averaged density at the outlet, as well as the density of gaseous ammonia (10 kg/m^3) and liquid ammonia (600 kg/m^3):

$$\rho_{avg} = X_g\rho_g + X_l\rho_l \tag{46}$$

with

$$X_l + X_g = 1. \tag{47}$$

For varying pressures at the outlet, Fig. 19 shows the discharge coefficient obtained. It varies from 0.05 when injecting in atmospheric conditions, to 0.2 when injecting in engine-relevant conditions. Going forward, the value of 0.2 is selected to simulate the discharge coefficient at the nozzle in the 1-D simulations.

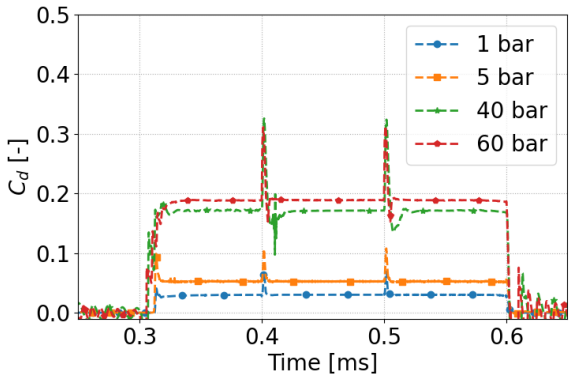

Figure 19: Time evolution of discharge coefficients during injection for different outlet pressures.

Simulation

The fuel tank holds 200 bar, compressing the fuel with nitrogen. The temperature in the tank is ambient. The injection is modeled by the fuel's pressure and temperature at the injection time, which are considered constant during the simulation. This is unrealistic as the injected fuel will mix with air, and the combustion will start. However, this assumption is necessary to focus on the dynamic of the injector itself and not on the engine's response. We will assume the combustion chamber temperature to be at 500 K and the pressure at 40 bar at time of injection. Range Kutta of second order is used to solve the equations. The covered simulation time is 3 ms, with the injection of the fuel lasting 1.25 ms. The time step is 1e-5 ms and is chosen to capture the system's dynamics while keeping the simulation within a reasonable time. The model is compared to a simulation by Zhang et al. [8]. The GDI in that publication differs slightly with the one considered in the present work as the needle lifted upwards at a maximum of 0.1 mm, while the injector described in this study can only raise 0.07 mm. This deviation is yet not considered significant. A comparison of the dimensionless needle lift is shown in Fig. 20 to account for this difference in maximum lift. The lift in the graph is normalized by the maximum needle lift of the respective injectors.

The needle lifts as a response to the electromagnetic force being more prominent than the downward forces such as the spring force, pressure from the fuel, etc., as shown in Fig. 21. The bumper model stops the needle when it is above its maximum displacement value or below its minimum displacement, as shown in Fig. 22. Slight oscillations occur at these positions, but equilibrium is reached quickly. The difference with the values reported in literature is minor and can be linked to the slightly different profile of electric potential supplied.

One objective of the model is to include pressure and temperature evolution through the injector to get the nozzle exit values without CFD. As described above two models were developed: one for gas and the other for liquid fuel. Results for both models are presented hereafter.

Gas fuel

For this simulation, the fuel used is methane, so our assumption of incompressible perfect gas holds at the conditions considered. The evolution of temperature and pressure are illustrated in Fig. 23 and

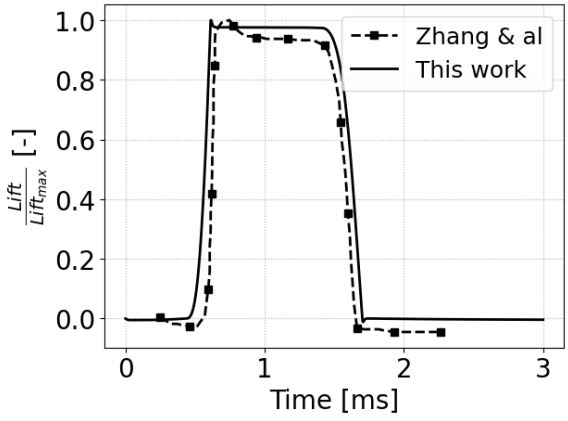

Figure 20: Time evolution of the normalized needle lift from the model developed in this paper and from [8]. The maximum lift value of each study is used for the normalization.

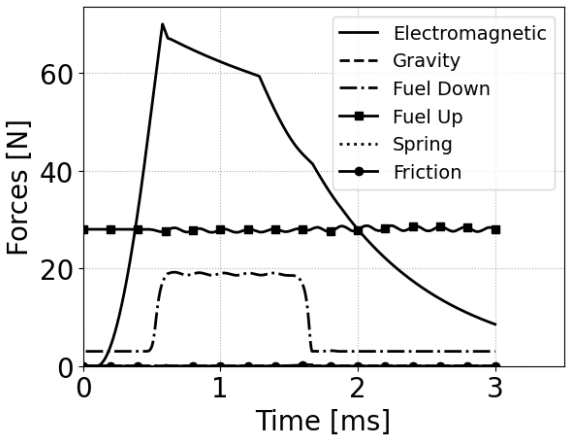

Figure 21: Time evolution of the forces acting on the needle. The force by the bumper is not pictured here.

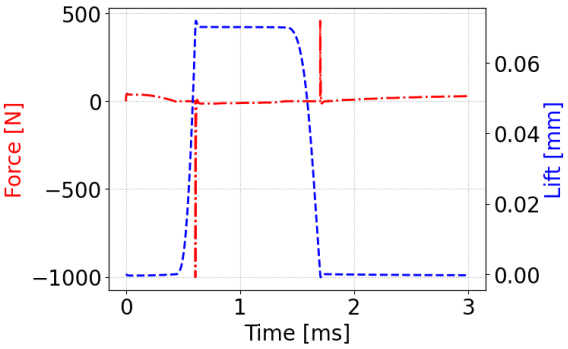

Figure 22: Time evolution of the needle lift (blue dashed line) and of the force acting on the needle induced by the bumper model (red dashed-dotted line).

Fig. 24 as well as the mass flow rate through the injector Fig. 25. The mass flow rate is compared with that of Zhang et al. [8] where CFD was used to obtain the fuel flow.

The injector geometry causes a pressure drop from the tank to the injector's exit of around 10 bar, as seen in Fig. 23. The fuel in the sac is around 188 bar, oscillating due to the pressure wave in the injector. The reached injection pressure still enables a high-pressure injection. The pressure in an intermediate chamber is pictured in Fig. 23 where the oscillations due to the pressure wave continue to travel inside the

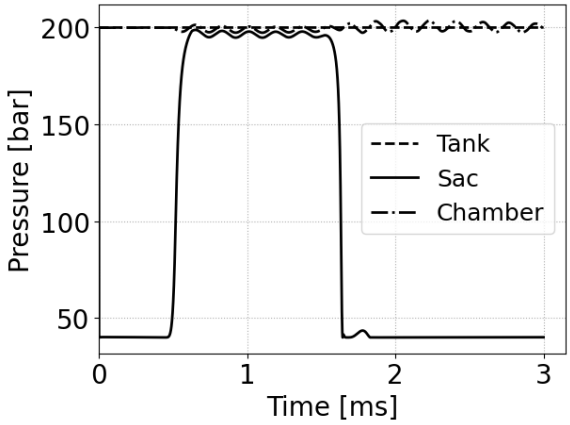

Figure 23: Time evolution of the pressure in the tank and out of the injector for the gaseous model.

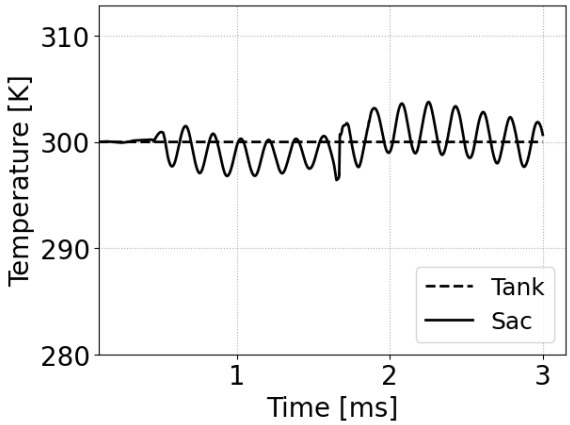

Figure 24: Time evolution of the temperature in the tank and out of the injector for the gaseous model.

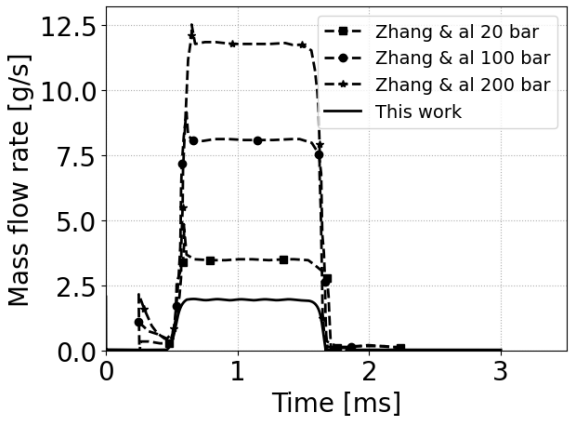

Figure 25: Time evolution of the mass flow out of the injector for the gaseous model. Comparison with [8] where a liquid fuel is used.

injector. This traveling wave impacts the needle and the sac's pressure even after the injector has closed, oscillating around 40 bar, although this is not visible in Fig. 23. The temperature shown in Fig. 24 oscillates around 300 K due to the pressure oscillation affecting the fluid's temperature following the perfect gas law. When the needle starts lifting, the temperature drops below the tank temperature. The fluctuations after the needle closes are due to the pressure wave oscillations still impacting the system. The mass flow injected is at around 0.001 kg/s for about 0.00125 s, reaching a total fuel mass of 1.25 mg in one injection. The predicted value differs significantly to the anticipated mass flow of fuel in Zhang et al. [8] at 200 bar, reporting a fuel mass of around 16 mg injected into the combustion chamber during one injection. The main difference between the compared systems is liquid fuel in the work by Zhang et al. and gaseous in our results. Hence in the next section, we verify that changing our model to liquid fuel allows to have comparable results as Zhang et al..

Liquid fuel

For this case, the fuel considered is liquid ammonia. It is liquid at 200 bar and ambient temperature, which are the tank's initial conditions for this simulation. As for the gas study, the evolution of the pressure, temperature and mass flow are computed (Fig. 26, Fig. 27 and 28 respectively)

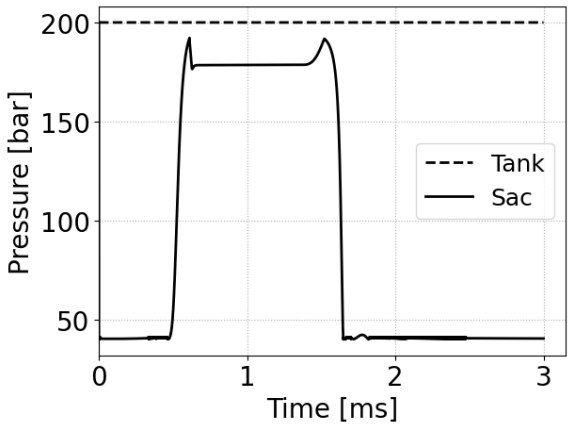

Figure 26: Time evolution of the pressure in the tank and out of the injector for the liquid model.

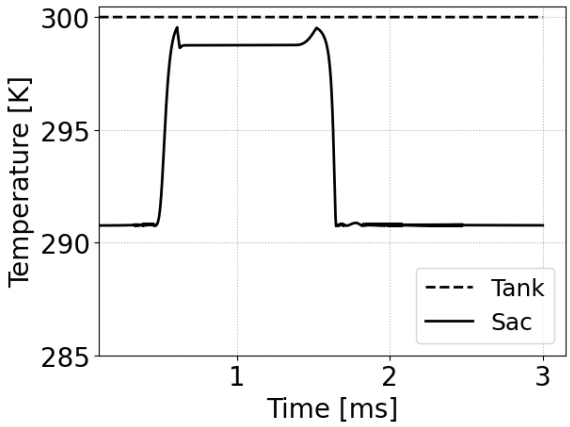

Figure 27: Time evolution of the temperature in the tank and out of the injector for the liquid model.

The computation time for the liquid model takes longer than that of the gas, as the model employs a procedure to use the thermodynamic tables from REFPROP. The pressure in the sac is initiated with that of the combustion chamber's pressure. Then, when the needle is lifted, a surge of fuel pushes the pressure to 190 bar. The pressure then stabilizes as the injection progresses at 180 bar. As the needle moves down, a second surge brings back the pressure to 190 bar before it reduces as the injector closes. The injection pressure is slightly lower than that reached with the gas system. Once the needle touches the nozzle's seat, a slight jump causes a minor pressure rise as in the gas case. The temperature in the sac converges to 290 K before the start of injection, which is likely linked to ammonia's cooling properties. When the injection starts, the temperature remains below 300 K. This

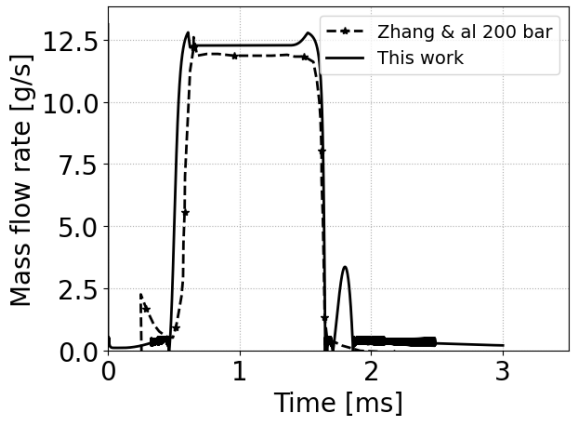

Figure 28: Time evolution of the mass flow out of the injector for the liquid model for an initial pressure in the tank of 200 bar. Comparison with [8] at the same pressure.

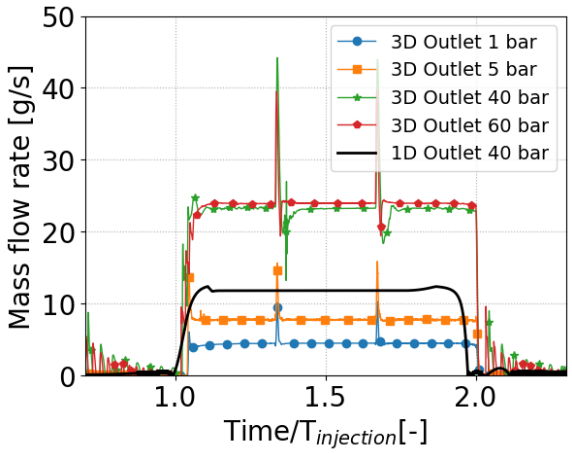

Figure 29: Time evolution of the mass flow rate out of the injector for the liquid model. Comparison with the time evolution of mass flow rate in the 3-D CFD simulations.

means that the fuel injected into the chamber will be at a lower temperature than the temperature at which the fuel is stored, this is something that will be important to account for when studying ammonia injection. The mass flow rate obtained is very close to the one from Zhang et al. [8] as seen in Fig. 28 despite the difference in the fuel's nature. However, due to the novelty of ammonia as a fuel, the literature still lacks of experimental investigations and validation data for injector flow of ammonia. The different fuel densities may also cause deviations in the predicted results and literature. The injector's geometry was kept the same as for the gaseous simulation, meaning that the difference in mass flow rate obtained in the gas case was indeed due to not accounting for the liquid nature of the fuel. In the liquid case, despite a model for pressure wave being included, no oscillations are captured with the model. The absence of a wave might be due to the flow's higher velocity, which can be seen in the high mass flow rate. No pressure oscillations were captured in Zhang et al. [8] either. A comparison with the 3-D CFD that was performed to investigate the discharge coefficient for ammonia is presented Fig. 29 and results show that the same order of magnitude for the liquid mass flow rate is reached. To compare the simulations, the time is normalized by the injection duration for each case. Indeed, the 1-D model does not account for multiphase flow, and this impacts the results and is believed to be the reason for the difference with the 3-D simulations as revealed in Fig. 29. This is also why no comparison with pressure and temperature is shown here. Nevertheless, to get an estimate of the mass flow rate and the response of the injection to the magnetic inputs, the 1-D model still has advantages, especially in terms of computational time. The 1-D models run in a few minutes whereas the 3-D CFD takes several hours on the same system.

It is worth noting that the injector model developed in this study accounts for the electromagnetic force and the needle displacement accurately compared to what is reported in literature. The needle lift and interaction with the fuel injection are good as there is no leakage, and the fuel flows when the needle is lifted. Both the gas and liquid models give realistic results. However, in order to capture even more physics, a third model would need to be developed to account for the fuel's gas and liquid phases in order to account for e.g. cavitation and other multiphase characteristics.

Conclusion

In this paper, a model of a solenoid injector was developed using the bond graph methodology. The model is divided into three sub-models for the electromagnetic, mechanical, and fluid systems respectively. The model accurately predicted the needle lift. The electromagnetic and mechanical model for the control of the needle was coupled to a fluid model using pseudo bond graphs to predict the fluid behavior in the injector. The evolution of the system's pressure, temperature, and mass flow rates were investigated using pseudo bond graphs and thermodynamic tables. Several levels of complexity were accounted for in the model, from the simple perfect gas law for gaseous fuels to linking the model to thermodynamic tables to account for liquid fuels. This model can be used to simulate various initial conditions and geometries. The initial conditions of pressure and temperature can be varied, as well as the power strategy to study varying input pulses for the solenoid and durations. A sensitivity study of the effect of the nozzle's hole diameter or the number of holes can be helpful given the immense diversity of solenoid injectors that exists, and the presented model has proven to be a sensible tool for rapid testing in the initial phases of injector development. Other fuels can be considered using the NIST database, and a model for a realistic combustion chamber could be linked to the injector model to study the interaction between injection and chamber.

Acknowledgement

The authors would like to acknowledge NTNU's Nanolab for the use of SEM equipment and assistance in realizing the silicone mold pictures. Convergent Science provided CONVERGE licenses and technical support for this work. This work is supported by the Norwegian Research Council and partners in the Low Emission Center.

References

1. G. Karl, R. Kemmler, M. Bargende, and J. Abthoff, "Analysis of a direct injected gasoline engine," *SAE Transactions*, vol. 106, pp. 835–847, 1997.

2. K. Shimotani, K. Oikawa, O. Horada, and Y. Kagawa, "Characteristics of gasoline in-cylinder direct injection engine," *JSAE Review*, vol. 17, no. 3, pp. 267–272, 1996.

3. V. Krivopolianskii, N. Lefebvre, S. Ushakov, and E. Pedersen, "Fuel rate curve-based reverse engineering approach for common rail diesel injectors," in *Automotive Technical Papers*, SAE International, sep 2019.

4. V. Aesoy and E. Pedersen, "Modeling and Simulation for Design and Testing of Direct Injection Gaseous Fuel Systems for Medium-Speed Engines," *SAE International Journal of Fuels and Lubricants*, vol. 4, no. 2, pp. 188–203, 2011.

5. Y. Bai, Q. Lan, L. Fan, X. Ma, and H. Liu, "Investigation on the fuel injection stability of high pressure common rail system for diesel engines," *International Journal of Engine Research*, vol. 22, no. 2, pp. 616–631, 2021.

6. W.-C. Tsai and T.-S. Zhan, "An experimental characterization for injection quantity of a high-pressure injector in gdi engines," *Journal of Low Power Electronics and Applications*, vol. 8, no. 4, 2018.

7. X. Yao, Z. Zhang, X. Kong, and C. Yin, "Dynamic response analysis and structure optimization of gdi injector based on mathematical model," *International Journal of Reliability, Quality and Safety Engineering*, vol. 25, no. 02, p. 1850008, 2018.

8. X. Zhang, A. Palazzolo, C. B. Kweon, E. Thomas, R. Tucker, and A. Kascak, "Direct fuel injector power drive system optimization," *SAE International Journal of Engines*, vol. 7, no. 3, pp. 1137–1154, 2014.

9. R. Payri, H. Climent, F. J. Salvador, and A. G. Favennec, "Diesel injection system modelling. methodology and application for a first-generation common rail system," *Proceedings of the Institution of Mechanical Engineers, Part D: Journal of Automobile Engineering*, vol. 218, no. 1, pp. 81–91, 2004.

10. C. Lhuillier, P. BREQUIGNY, C. Rousselle, and F. Contino, "Combustion characteristics of ammonia in a modern spark-ignition engine," in *Conference on Sustainable Mobility*, SAE International, oct 2019.

11. C. Lhuillier, P. Brequigny, F. Contino, and C. Mounaïm-Rousselle, "Experimental study on ammonia/hydrogen/air combustion in spark ignition engine conditions," *Fuel*, vol. 269, p. 117448, 2020.

12. S. Oh, C. Park, S. Kim, Y. Kim, Y. Choi, and C. Kim, "Natural gas–ammonia dual-fuel combustion in spark-ignited engine with various air–fuel ratios and split ratios of ammonia under part load condition," *Fuel*, vol. 290, p. 120095, 2021.

13. V. Macian, V. Bermudez, R. Payri, and J. Gimeno, "New technique for determination of internal geometry of a diesel nozzle with the use of silicone methodology," *Experimental Techniques*, vol. 27, no. 2, pp. 39–43, 2003.

14. D. Karnopp, D. Margolis, and R. Rosenberg, *System Dynamics: Modeling, Simulation, and Control of Mechatronic Systems*. EngineeringPro collection, Wiley, 2012.

15. C. Kleijn, M. Groothuis, and H. Differ, "20-sim 4.4 reference manual," 2013.

16. N. Hogan, "Example : Electromagnetic solenoid," tech. rep., 2002.

17. D. Karnopp, "State Variables and Pseudo Bond Graphs for Compressible Thermofluid Systems," *Journal of Dynamic Systems, Measurement, and Control*, vol. 101, pp. 201–204, 09 1979.

18. V. Siderius, D. Krekelberg, W. Hatch, and H. Shen, "Nist standard reference simulation website," 2022.

19. E. Pedersen, "Modelling Multicomponent Two-Phase Thermodynamic Systems Using Pseudo-Bond Graphs," in *Proc. of the 5th International Conference on Bond Graph Modeling,*, Society for Computer Simulation International, 2001.

20. K. Strand and H. Engja, "Bond graph interpretation of one-dimensional fluid flow," *Journal of the Franklin Institute*, vol. 328, no. 5, pp. 781–793, 1991.

21. E. W. Lemmon, I. H. Bell, M. L. Huber, and M. O. McLinden, "NIST Standard Reference Database 23: Reference Fluid Thermodynamic and Transport Properties-REFPROP, Version 10.0, National Institute of Standards and Technology," 2018.

22. X. Li, Y. Cheng, S. Ji, X. Yang, and L. Wang, "Sensitivity analysis of fuel injection characteristics of gdi injector to injector nozzle diameter," *Energies*, vol. 12, no. 3, 2019.

23. M. Lebrun, "Normal modes in hydraulic lines," in *1984 American Control Conference*, pp. 458–467, 1984.

24. J. U. Thoma and D. B. Richter, "Simulation of Fluid Pipes in Hydrostatic Circuits Using Modal and Segmented Methods," *Transactions of the Society for Computer Simulation International*, vol. 3, pp. 337–349, 1986.

25. J. Gaucherand, C. Netzer, M. T. Lewandowski, and T. Løvås, "Modelling of liquid injection of ammonia in a GDI injector using RANS simulation [submitted for publication]," *63rd International Conference of Scandinavian Simulation Society*, 2022.

26. K. J. Richards, P. K. Senecal, and E. Pomraning, "Converge manual v3.0," 2017.

27. B. Shields, K. Neroorkar, and D. P. Schmidt, "Cavitation as rapid flash boiling," *ILASS-Americas 23rd Annual Conference on Liquid Atomization and Spray Systems, Ventura, CA, May 2011*, 2011.

28. Z. Bilicki, J. Kestin, and J. T. Stuart, "Physical aspects of the relaxation model in two-phase flow," *Proceedings of the Royal Society of London. A. Mathematical and Physical Sciences*, vol. 428, no. 1875, pp. 379–397, 1990.

29. A. A. Amsden, "Kiva-3v: A block-structured kiva program for engines with vertical or canted valves," tech. rep., 7 1997.

Contact Information

Jessica Gaucherand, Ph.D.
jessica.gaucherand@ntnu.no